Progress In Electromagnetics Research, Vol. 138, 697–715, 2013

A PLANAR PRINTED ANTENNA ARRAY EMBEDDED IN THE WING STRUCTURE OF A UAV FOR COMMUNICATION LINK ENHANCEMENT

Mohammad S. Sharawi[1, *], Mohamed Ibrahim[1], Sameir Deif[1], and Daniel N. Aloi[2]

[1]Electrical Engineering Department, King Fahd University of Petroleum and Minerals, Dharan 31261, Saudi Arabia

[2]Electrical and Computer Engineering Department, Oakland University, Michigan, Rochester, USA

Abstract—In this work a 12-element patch planar antenna array is designed, fabricated and tested along with its radio frequency (RF) feed network at 2.45 GHz. The array is designed to be embedded in the wing structure of a fixed wing hobby-type UAV. The planar array allows for beam steering with two degrees of freedom (θ_b, ϕ_b). The maximum mutual coupling between antenna elements was -25 dB. The RF combiner was phase compensated to minimize the phase imbalance between its branches. The maximum measured antenna gain was 21.4 dB. The 3D radiation pattern at several steering angles was measured at an outdoor antenna range facility. Measured and simulated values were in good agreement.

1. INTRODUCTION

Unmanned aerial vehicles (UAV) have a lot of applications in military as well as civil sectors. UAV applications includes search and rescue [1–3], traffic monitoring [4], mapping [5, 6], remote sensing [7–11], surveillance [12–14], and even wireless communications relays [15, 16]. Any UAV has two wireless communication links with its ground station, a control link [17] and a data link [18–21]. The control link usually has a long operating range due to its relatively low frequency of operation, while the data link has a shorter range due to its higher frequency of operation. The data link is used in transmitting sensory data to the ground station for further processing and logging.

Received 18 February 2013, Accepted 15 April 2013, Scheduled 17 April 2013

* Corresponding author: Mohammad S. Sharawi (msharawi@kfupm.edu.sa).

Antenna array designs for UAVs are constrained by the vehicle's mechanical dimensions, payload, and the materials used to cover the vehicle's structure (whether they are conducting or non-conducting materials). In this work a hobby-type UAV called the mini-telemaster [22] is considered.

Embedding the antenna inside the structure of the vehicle enhances the aerodynamic profile of the vehicle and reduces air drag compared to external parasitic antennas. It also extends the lifetime of the radiating elements because they will not be subjected to harsh environmental conditions. Embedded antennas have been proposed and studied in a number of previous works, where in [23], a uniform linear monopole antenna array was embedded inside the wing as a part of its mechanical structure. Four elements and 8 elements were modeled, simulated and studied. A single monopole was printed on the wing rib with $20.8 \times 38 \times 0.8\,\text{mm}^3$ size. The frequency of operation was 2.4 GHz and the array was linear. Thus beam steering was not possible with more than one degree of freedom (DOF). In [24] the 4-element linear array proposed in [23] was tested and measured. Planar antenna arrays can provide two degrees of freedom with different polarizations and allow for spacial scanning as was shown in different applications in [25–27]. In [28], a 14-element planar patch antenna array was proposed for UAV applications. The array size was $462 \times 116 \times 0.8\,\text{mm}^3$ and weighted 122.5 gm.

In [29] an 8-element linear antenna array was employed successfully within a high altitude long endurance platform (HALE) in order to localize mobile terminals with an accuracy of about 1.2 m by estimating the angle of arrival (AOA) of the received signal. It is worth mentioning that estimating the AOA requires a separate receiver for each antenna element. The proposed antenna array in this work will target the enhancement of the communication link between the flying vehicle and its ground station. Thus only one transceiver and an RF feed network are required. In [30], a 4×12 microstrip patch antenna array was developed for an L-band repeat-pass interferometric synthetic aperture radar (InSAR) at 1.2575 GHz with bandwidth 80 MHz in order to provide accurate topographic maps. 24 transceivers were used in this work to facilitate beam scanning in the azimuth direction for a range of $\pm 20^\circ$. In [31], an adaptive vertical antenna array was proposed for a wireless broadband (WiBro) modem for a UAV communication system to overcome the altitude limitation of the UAV caused by restricted antenna coverage of the WiBro base-station, a 5×5 planar array at 2.5 GHz was simulated and a phase correction system was proposed in order to compensate for the UAV's attitude in 3D space by utilizing a gyro sensor and an

accelerometer. No fabricated prototypes were presented. In [32], a 35×7 single-polarized probe fed Ku-band patch array operating at 16–18 GHz was presented. The single element radiation pattern was simulated and measured. However the collective total radiation pattern of the array was not addressed.

In this work we propose the design and fabrication of a 12-element planar patch antenna array along with its RF feed network to be embedded within the wing structure of a small size UAV for communication link enhancement. The array operates at 2.45 GHz and weighs 105 gm. The feed network consists of a phase balanced 12-port combiner and phase shifters. The fabricated prototype consisting of the antenna array and the feed network was characterized in an outdoor antenna range facility at Oakland University (Michigan, USA). The effect of the beam direction on the HPBW and the gain was studied in detail. The contributions of the work can be summarized as follows:

1) The design and implementation of a planar antenna array to be embedded within the wing structure of a small size UAV.
2) A small size-custom made combiner with optimized phase response for the planar antenna array.
3) The system level integration of the antenna array within the structure of the UAV and the combiner within a controlled beam steering environment and the characterization of the behavior of this beam-steering capability on the UAV for communication link enhancement via the study of the steering angles on the HPBW and gain in the space of coverage.

The rest of the paper is organized as follows, in Section 2, the system level model of our proposed on UAV beam-steering capability is discussed. In Section 3, simulation, modeling and measurement results are presented. A detailed discussion of the obtained results within the context of the system level architecture proposed is presented in Section 3 as well. Finally, Section 4 concludes the paper.

2. SYSTEM MODEL

The system proposed in this work consists of a planar printed antenna array a phase controlled RF feed network, a combiner/splitter (C/S) and a transceiver. Figure 1 shows the block diagram of the system. The antenna array is connected through RF lines (coaxial cables) to the feed network whose job is to control the phases of the signals fed to individual elements. The feed network is then connected to the C/S whose function is to combine the signals of the 12 elements together and feed them to the transceiver. The antenna array is composed

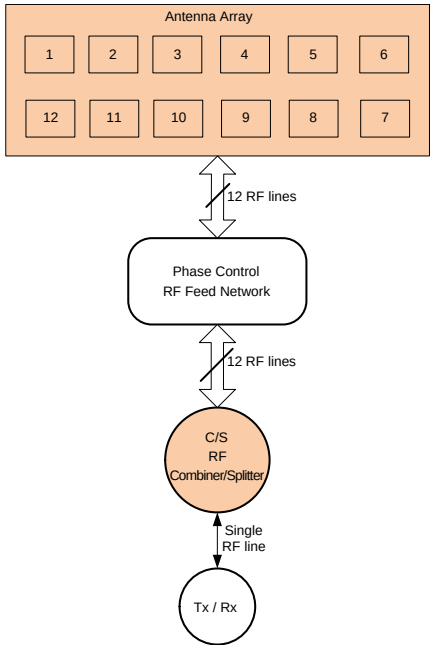

Figure 1. System block diagram.

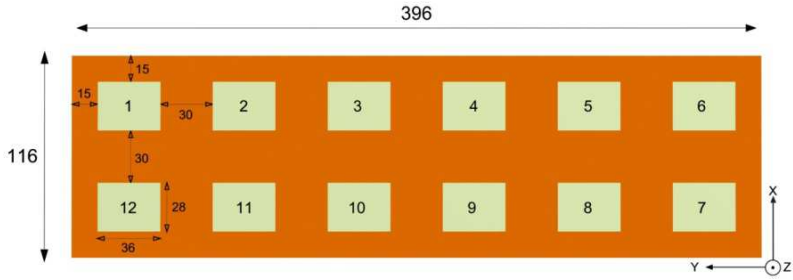

Figure 2. Designed planar 2×6 antenna array (all dimensions are in mm).

of 12 printed rectangular identical patch elements each with a size of $36 \times 28\,\text{mm}^2$, and the array total size is $396 \times 116\,\text{mm}^2$ as shown in Figure 2. The antenna array was printed on an FR-4 material with two copper layers (front and back) of thickness 36 µm. The substrate material had a relative permittivity (ε_r) of 4.4. The substrate thickness was 0.8 mm The frequency of operation was 2.45 GHz. All the antenna parameters are summarized in Table 1.

Table 1. The design parameters for the 2×6 antenna array.

Parameter	Value	Units
Substrate width	66	mm
Substrate length	58	mm
Patch width	36	mm
Patch length	28	mm
Substrate permittivity ε_r	4.4	unit less
Thickness of copper layer	36	µm
Thickness of substrate	0.8	mm
Inter-element spacing d_x	30	mm
Inter-element spacing d_y	30	mm
Frequency	2.45	GHz
Weight	105	gm

A compact size 12-port power C/S was designed and fabricated on an FR-4 material with 0.8 mm substrate thickness. The total size of the board was $78.5 \times 61 \times 0.8\,\text{mm}^3$. The phase imbalance due to the internal IC phase imbalance was minimized by careful PCB design and phase compensation. 3-way and 4-way power C/S Integrated Circuits (IC) were used; the SCN-3-28+ [33], and the BP4U1+ [34]. The maximum phase imbalance between the SCN-3-28+ ports was 8° and it was 28° for the BP4U1+ according to the vendor specifications. SMA connectors were connected to the I/O ports. All footprints of the components were made manually using a PCB design tool. Three external resistors that were connected to the output ports for isolation purposes of the 3-port combiner were used with values of 124 Ω and 127 Ω. All microstrip lines were made with 50 Ω impedance. The schematic of the C/S is shown in Figure 3.

3. RESULTS

3.1. Simulation Results

To check the resonant frequency of the single patch element, the reflection coefficient (S_{11}) is plotted in Figure 4 where the resonant frequency was almost at 2.45 GHz and the −10 dB bandwidth was 50 MHz.

The radiation pattern was generated first for a single patch using HFSS [35], then the patch patterns were combined together (array

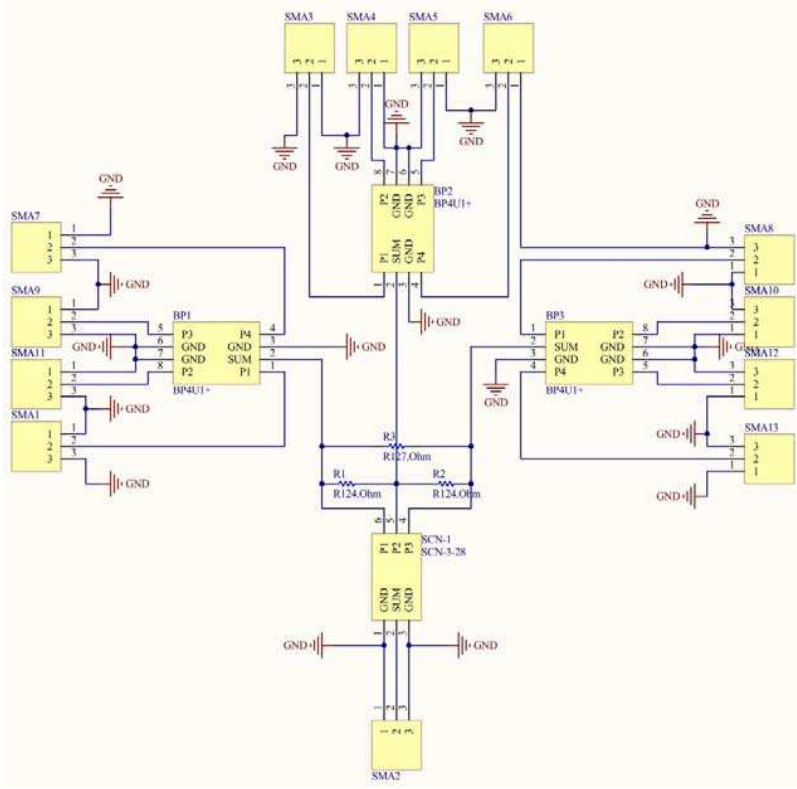

Figure 3. The schematic diagram of the 12-port combiner/splitter circuit.

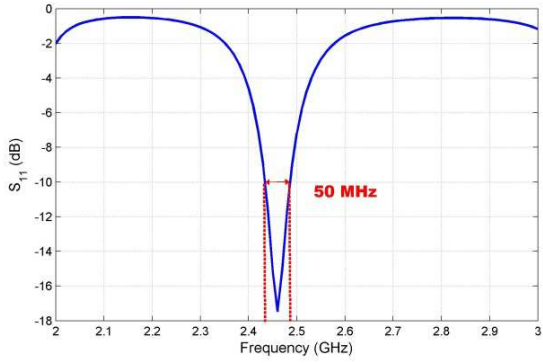

Figure 4. The simulated reflection coefficient (S_{11}).

pattern multiplication) according to Equation (1) using Matlab [36] to produce the total radiation pattern

$$\text{Gain}_{\text{total dB}}(\theta,\phi) = \text{Array Factor}_{\text{dB}}(\theta,\phi) + \text{Gain}_{\text{single patch dB}}(\theta,\phi) \quad (1)$$

The computation of the antenna array radiation pattern according to Equation (1) must be validated by good isolation between neighboring elements. Thus the mutual coupling must be quantified by measuring the S-parameters, these measurements are presented in the next section.

The radiation pattern of the given planar array can be steered by controlling the phases of the signal feed for each element. Thus a phase controlled feed network is needed. This will allow beam steering with two DOF and with the help of a beam steering algorithm; the maximum gain point (θ_b, ϕ_b) in the radiation pattern could be steered directly to the direction of the maximum received signal strength (RSS). However developing a beam steering algorithm is not the scope of this work.

The normalized 3D contour plot of the gain pattern is shown in Figure 5 with zero inter-element progressive phases. The main lobe has a relatively small half power beam width (HPBW) in the y-direction compared to the x-direction. This is because in the y-direction the array has 6 elements, while in the x-direction it has only 2 elements.

The radiation pattern is a function of the beam steering angles

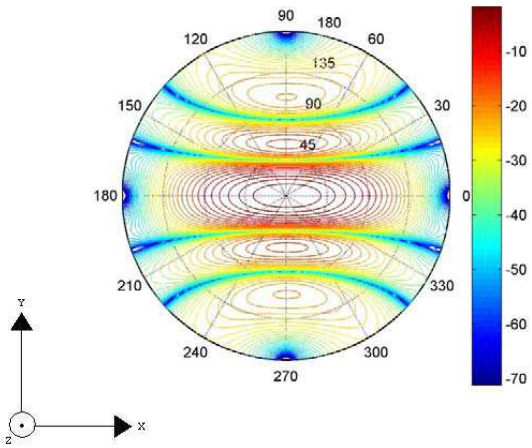

Figure 5. A colored contour plot of the normalized radiation pattern (in dB) of the proposed 2×6 antenna array at ($\theta_b = 0°$, $\phi_b = 0°$). The circular axis represents ϕ and the radial distance represents θ, at the center $\theta = 0°$, and at the edge $\theta = 180°$.

(θ_b, ϕ_b). Thus for each value of (θ_b, ϕ_b) we will have a different radiation pattern which describes the antenna gain and the HPBW at each point in the spherical space $(0^\circ < \theta \leq 180^\circ, 0^\circ < \phi \leq 360^\circ)$ around the antenna. To steer the beam to a specific (θ_b, ϕ_b) direction, a uniform amplitude distribution is used while the progressive phase between the adjacent elements in the x and y directions was changed according to,

$$\beta_x = -kd_x \sin\theta_b \cos\phi_b \tag{2}$$

$$\beta_y = -kd_y \sin\theta_b \sin\phi_b \tag{3}$$

where β_x, β_y are the progressive phases in the x and y directions, respectively, k is the wave number, d_x and d_y are the inter-element spacings in the x and y directions. The HPBW was quantified in both directions (θ and ϕ) for all possible steering angles (θ_b, ϕ_b). The characterization of the HPBW in θ-direction ($HPBW_\theta$) is shown in Figure 6, while the HPBW in ϕ-direction ($HPBW_\phi$) is shown in Figure 7. It is worth mentioning that the minimum HPBW achieved in the θ-axis is 18° and in the ϕ-axis is 32°.

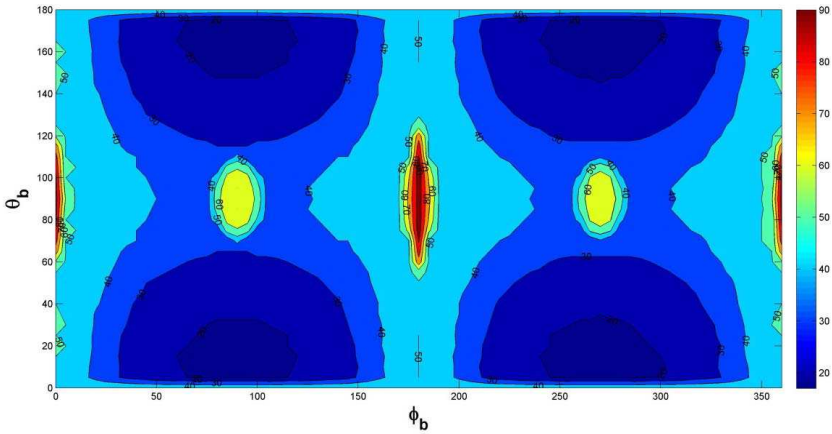

Figure 6. A colored contour plot of HPBW as an angular cut (deg) along the θ axis for $(0^\circ < \theta_b < 180^\circ)$ and $(0^\circ < \phi_b < 360^\circ)$.

The minimum $HPBW_\theta$ regions exist between $(60^\circ < \phi_b < 120^\circ)$ and $(240^\circ < \phi_b < 300^\circ)$ on the ϕ_b-axis and between $(5^\circ < \theta_b < 32^\circ)$ and $(147^\circ < \theta_b < 175^\circ)$ on the θ_b-axis. The minimum $HPBW_\phi$ regions exist between $(0^\circ < \phi_b < 75^\circ)$, $(105^\circ < \phi_b < 255^\circ)$ and $(285^\circ < \phi_b < 360^\circ)$ in the ϕ_b-axis and between $(20^\circ < \theta_b < 160^\circ)$ in the θ_b-axis. Keep in mind that the actual regions are not squarely

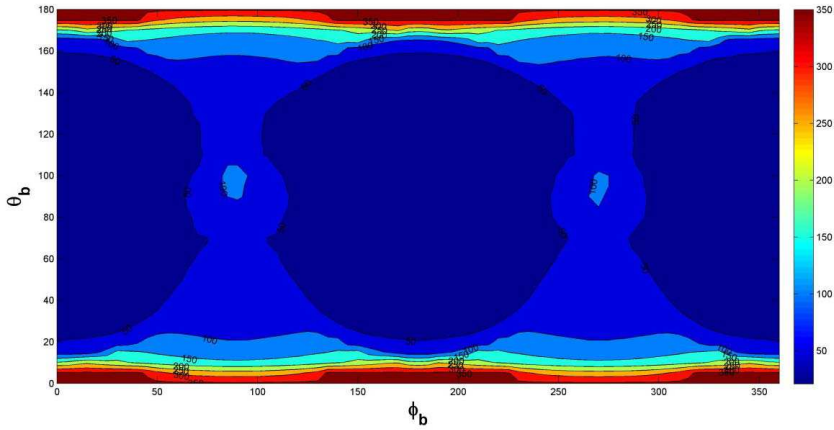

Figure 7. A colored contour plot of HPBW as an angular cut (deg) along the ϕ axis for $(0^\circ < \theta_b < 180^\circ)$ and $(0^\circ < \phi_b < 360^\circ)$.

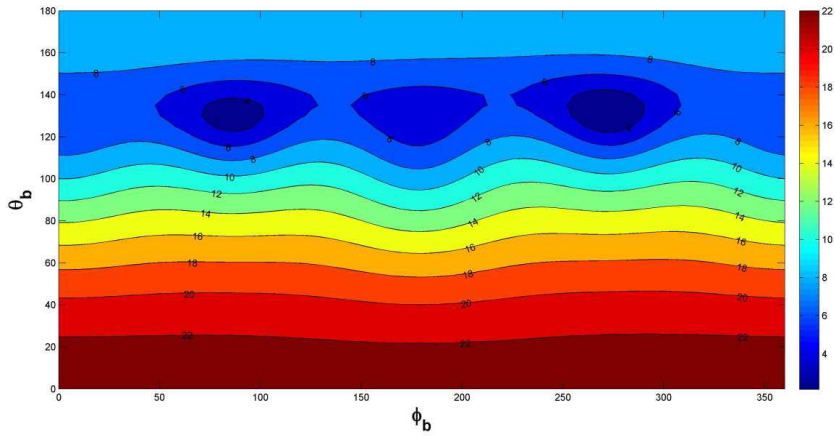

Figure 8. A colored contour plot showing the maximum gain produced at each given steering angles (θ_b, ϕ_b).

shaped. Thus not all points in the region belong to the minimum HPBW category.

The pointing gain is the antenna gain produced exactly at the given beam steering angles $G(\theta = \theta_b, \phi = \phi_b)$. The pointing gain was characterized for all beam steering angles and is shown in Figure 8, where the region of maximum pointing gain is found between $(0^\circ <$

$\phi_b < 360°$) in ϕ_b-axis and between ($0° < \theta_b < 22°$) in θ_b-axis. The maximum simulated pointing gain produced was 22 dB. The region of minimum pointing gain is found in ($120° < \theta_b < 140°$) in θ_b-axis and in ($70° < \phi_b < 100°$) and ($250° < \phi_b < 290°$) in ϕ_b-axis. The minimum pointing gain was 4 dB. The quantification of maximum gain and HPBW is important for this application as it will determine the maximum range and steering angle beyond which the array and its beam steering capability will not be beneficial.

The simulation model for the C/S was made using Microwave Office (MWO). The measured *s*-parameter files for the two component models were obtained from the vendor [33, 34]. The simulation model was optimized to compensate for the internal phase and amplitude imbalances that are within the ICs. In the simulation model, phase compensation was performed to minimize the effect of these imbalances. This is because their effect cannot be removed completely as they vary from chip to chip. Simulation results are presented along with the measured ones in the following section.

3.2. Measured Results

The fabricated model of the planar antenna array is shown in Figure 9. Figure 10 shows the array attached to the bottom side of the UAV's wing. Another copy of the fabricated antenna board was attached to the other wing to provide balance between the two wings. The skeleton of the UAV is shown as the array will be wrapped with plastic sheets to be attached to the UAV structure. The UAV was made of balsa wood as it is a small hobby type one. The single array weighted 105 gm, thus both will add 210 gm of load weight to the UAV payload.

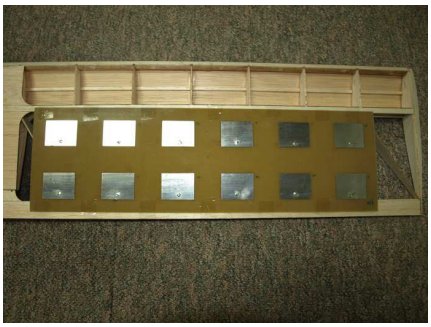

Figure 9. The 2×6 array attached to the wing structure of the UAV.

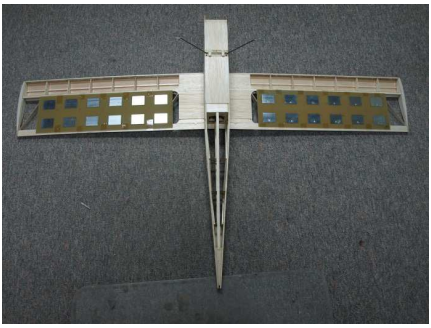

Figure 10. The fabricated antenna boards attached to the bottom of the UAV wing structure.

A series of s-parameters measurements were made using a vector network analyzer (VNA), an HP8510C. As shown in Figure 2, a number has been assigned to each element in the array; these numbers are then used in the s-parameters characterization in order to match between what was measured in the lab and what is shown in Figure 2. Figure 11 shows the measured reflection coefficients of the first 6 elements in the array. A minimum -10 dB band width of 40 MHz was obtained. The measured resonant frequency was 2.48 GHz for all antennas. Figure 12 shows mutual coupling curves between several adjacent element combinations. The worst coupling case obtained was -25 dB.

The fabricated compact size 12-port power combiner/splitter is shown in Figure 13. The simulated and measured results for all paths

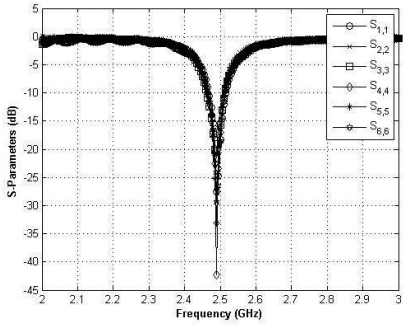

Figure 11. Measured reflection coefficient for patch elements; 1, 2, 3, 4, 5, and 6.

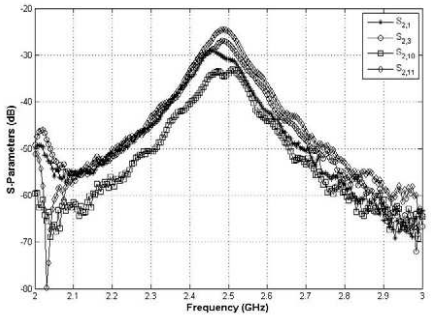

Figure 12. Measured coupling between elements (2, 1), (2, 3), (2, 10), and (2, 13).

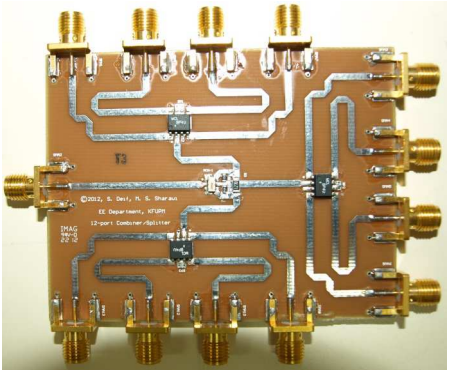

Figure 13. The fabricated C/S PCB.

Table 2. Simulated and measured C/S results.

Groups	Ports	Measured Results (V1)		Simulation (compensated)		Measured Results (V2)	
		Amplitude (dB)	Phase (degree)	Amplitude (dB)	Phase (degree)	Amplitude (dB)	Phase (degree)
G1	Port 01	−14.86	52.48	−12.21	112	−11.53	59.93
	Port 02	−14.25	24.13	−12.51	112	−11.02	70.81
	Port 03	−13.96	25.58	−12.63	112	−10.96	71.27
	Port 04	−14.71	34.24	−12.63	112	−11.15	66.94
G2	Port 05	−13.29	70.99	−12.4	113	−11.89	70.74
	Port 06	−12.55	45.84	−12.83	113	−11.03	77.92
	Port 07	−12.9	45.28	−12.7	113	−10.94	78.99
	Port 08	−12.96	53.05	−12.7	113	−11.08	74.97
G3	Port 09	−14.61	56.26	−12.16	112	−11.19	63.45
	Port 10	−13.84	30.68	−12.47	112	−11.14	77.94
	Port 11	−13.54	28.18	−12.59	112	−11	68.21
	Port 12	−14.05	36.12	−12.59	112	−10.86	69.06
Max		−12.55	70.99	−12.16	113	−10.86	78.99
Min		−14.86	24.13	−12.83	112	−11.89	59.93
Max. dev.		2.31	46.86	0.67	1	1.03	19.06
G1 dev.		0.9	28.35	0.42	0	0.57	11.34
G2 dev.		0.74	25.71	0.43	0	0.95	8.25
G3 dev.		1.07	28.08	0.43	0	0.33	14.49

are shown in Table 2. Two versions of the board were fabricated. Version 1 (V1) was made with equal RF lines between all ports and the ICs. The measured phase imbalance was seen to be with a maximum of 47°. A second version was first modeled and simulated with phase compensated RF lines and after eliminating the phase difference in simulations, a second version (V2) of the board was fabricated. The phase imbalance was reduced by approximately 60% in V2. The phase imbalance cannot be totally eliminated as the ICs vendor specifications provide a range of imbalance that differs from one IC to another.

Figure 14 shows simulated and measured amplitude and phase

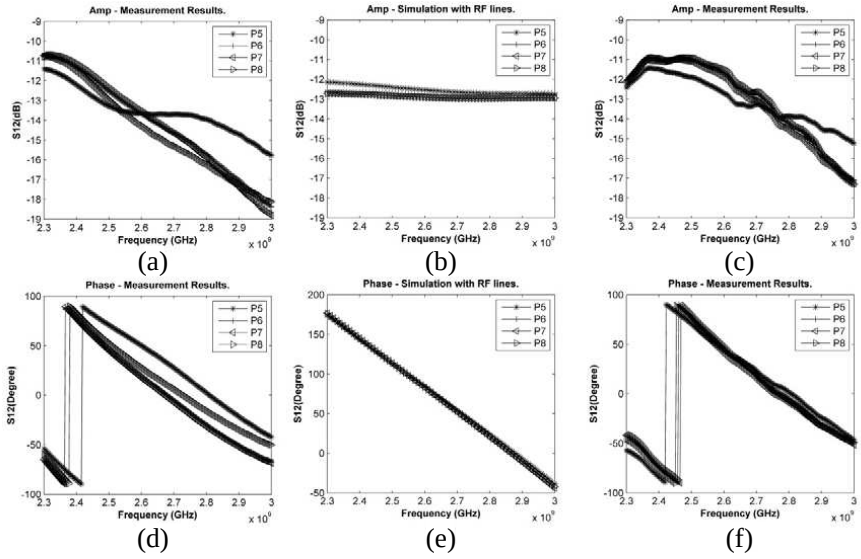

Figure 14. Simulation and measured results of the C/S. (a), (d) Amplitude and phase for measured results without compensation (V1). (b), (e) Simulation after phase compensation. (c), (f) The measured results after compensation (V2).

curves for 4-paths (5–8) in the frequency range covering 2.3–3 GHz. The measured amplitude and phase for the first design (V1) are shown in Figures 14(a) and (d), respectively. One can notice that the internal phase imbalance of the ICs is obvious in the results. A deviation of almost 25–28° in phase between the 4-ports is clearly shown. In this design (V1), the lengths of all paths were kept the same. In MWO, we tried to compensate the phase imbalance of the design by adjusting the microstrip line lengths. Based on the measured results obtained from V1, Figure 14(e) shows a perfect phase balance, but this cannot be guaranteed with the fabricated model, where the phase imbalance of the ICs can change every time from a model to another. Thus, as shown in Figure 14(f), the fabricated version (V2) with phase compensation show an imbalance that is 60% smaller than V1. The amplitude imbalance for the simulated and measured results had good agreement and the maximum deviation was about 1 dB at the resonant frequency. The fabricated model of the 12-way power C/S occupied only $7.8 \times 6\,\text{cm}^2$ of board area, and weighed 36 gm.

The measured radiation patterns were conducted at an outdoor antenna range facility at Oakland University, Michigan, USA. The

measurement setup is shown in Figure 15. The antenna array was placed on a 1.7 m plastic stand above a 6 m diameter metal turn table. The transmitting antenna (a quad-ridge horn) was mounted on a 9 m half arch gantry. The array elements were fed with coaxial cables of different lengths to provide the appropriate inter-element phases for testing the beam steering capability of the array. RG316 cables were connected to the designed C/S (V2) and fed back to the measurement setup to measure the gain pattern. Four different steering angle configurations were tested due to the long collection times for 3D radiation patterns and limited cables. The expected steering values of the array (θ_b, ϕ_b) for each configuration are presented in Table 3.

Figure 15. Antenna range setup (Oakland University, Michigan, USA).

Table 3. Beam steering angles configurations.

Configuration	θ_b	ϕ_b
A	0°	0°
B	35°	45°
C	62°	26.6°
D	23.4°	0°

The measured 3D normalized gain patterns of configurations A-D are shown in Figures 16–19 respectively. Due to imperfections in the cables and inaccuracy of cutting each cable exactly at the desired length, the measured maximum gain regions in some of the configuration are a little bit shifted from the desired value of (θ_b, ϕ_b)

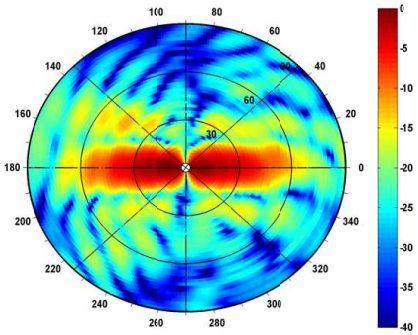

Figure 16. Measured normalized radiation pattern, configuration A, vertical polarization, the circled "X" represents ($\theta_b = 0°$, $\phi_b = 0°$).

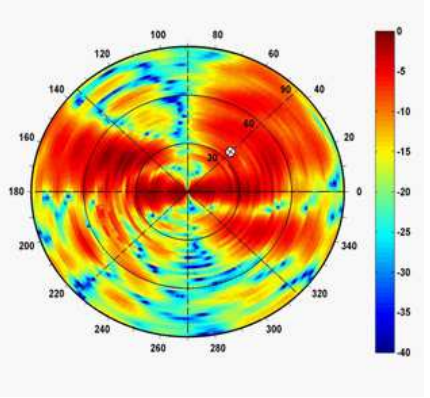

Figure 17. Measured normalized radiation pattern, configuration B, vertical polarization, the circled "X" represents ($\theta_b = 35°$, $\phi_b = 45°$).

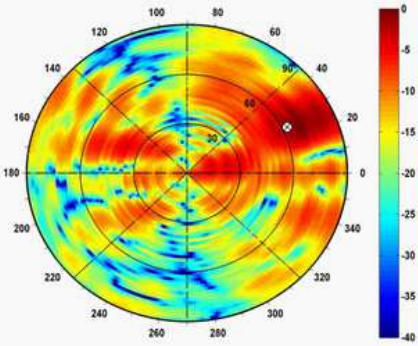

Figure 18. Measured normalized radiation pattern, configuration C, vertical polarization, the circled "X" represents ($\theta_b = 62°$, $\phi_b = 26.6°$).

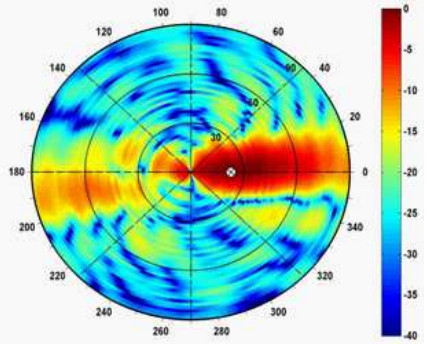

Figure 19. Measured normalized radiation pattern, configuration D, vertical polarization, the circled "X" represents ($\theta_b = 23.4°$, $\phi_b = 0°$).

which is denoted in the plots by a circled mark "X". Notice that at a frequency of 2.48 GHz the wave length $\lambda = 0.121$ m. Thus 1 mm $= 0.0083\lambda$, therefore an error of ± 5 mm in the cable length will result in a shift of $\pm 14.868°$ in the desired phase. In addition,

the combiner board has its own phase imbalance which adds to the inaccuracy of the beam direction. In general, the beams were in the vicinity of the desired steering angles. The maximum measured gain was 21.4 dB after subtracting the insertion loss from the cables (≈ -1.5 dB) and the combiner board (≈ -11 dB).

4. CONCLUSIONS

In this work we presented the design and implementation of a 2×6 printed patch antenna array ($39.6 \times 11.6\,\text{cm}^2$) and its compact size ($7.8 \times 6\,\text{cm}^2$) 12-way power combiner/splitter (C/S) to be embedded within the wing structure of a UAV for enhancing its communication link. Measured and simulation results were in good agreement. The system beam steering capability was characterized in an antenna range facility. The proposed design can be easily integrated within small size UAVs.

ACKNOWLEDGMENT

The authors would like to acknowledge the support provided by King Abdulaziz City for Science and Technology (KACST) through the science & technology unit at King Fahd University of Petroleum & Minerals (KFUPM) for funding this work through project No. 11-ELE2150-04 as part of the national science, technology and innovation plan (NSTIP).

REFERENCES

1. Naidoo, Y., R. Stopforth, and G. Bright, "Development of an UAV for search & rescue applications," *IEEE AFRICON*, 1–6, 2011.
2. Rudol, P. and P. Doherty, "Human body detection and geolocalization for UAV search and rescue missions using color and thermal imagery," *IEEE Aerospace Conference*, 1–8, 2008.
3. Lin, L. and M. A. Goodrich, "HAV intelligent path planning for wilderness search and rescue," *IEEE/RSJ International Conference on Intelligent Robots and Systems (IROS)*, 709–714, 2009.
4. Puri, A., K. P. Valavanis, and M. Kontitsis, "Statistical profile generation for traffic monitoring using real-time UAV based video data," *Mediterranean Conference on Control Automation (MED)*, 1–6, 2007.

5. Wang, F., Y. Wu, and Q. Zhang, "UAV borne real-time road mapping system," *Urban Remote Sensing Event*, 1–7, 2009.
6. Lin, Y., J. Hyyppä, and A. Jaakkola, "Mini-UAV-borne LIDAR for fine-scale mapping," *IEEE Geoscience and Remote Sensing Letters*, Vol. 8, No. 3, 426–430, May 2011.
7. Duan, Y., L. Yan, Y. Xiang, Z. Gou, W. Chen, and X. Jing, "Design and experiment of UAV remote sensing optical targets," *International Conference on Electronics, Communications and Control (ICECC)*, 202–205, 2011.
8. Hongying, Z., Y. Lei, G. Zhiyang, and Z. Lifu, "The characteristic analyses of images from the UAV remote sensing system," *IEEE International Conference on Geoscience and Remote Sensing Symposium (IGARSS)*, 3349–3351, 2006.
9. Sheng, H., H. Chao, C. Coopmans, J. Han, M. McKee, and Y. Chen, "Low-cost UAV-based thermal infrared remote sensing: Platform, calibration and applications," *IEEE/ASME International Conference on Mechatronics and Embedded Systems and Applications (MESA)*, 38–43, 2010.
10. Zang, W., J. Lin, Y. Wang, and H. Tao, "Investigating small-scale water pollution with UAV remote sensing technology," *World Automation Congress (WAC)*, 1–4, 2012.
11. Koo, V. C., Y. K. Chan, G. Vetharatnam, M. Y. Chua, C. H. Lim, C.-S. Lim, C. C. Thum, T. S. Lim, Z. bin Ahmad, K. A. Mahmood, M. H. Bin Shahid, C. Y. Ang, W. Q. Tan, P. N. Tan, K. S. Yee, W. G. Cheaw, H. S. Boey, A. L. Choo, and B. C. Sew, "A new unmanned aerial vehicle synthetic aperture radar for environmental monitoring," *Progress In Electromagnetics Research*, Vol. 122, 245–268, 2012.
12. Semsch, E., M. Jakob, D. Pavlicek, and M. Pechoucek, "Autonomous UAV surveillance in complex urban environments," *IEEE/WIC/ACM International Joint Conferences on Web Intelligence and Intelligent Agent Technologies (WI-IAT)*, Vol. 2, 82–85, 2009.
13. Kontitsis, M., K. P. Valavanis, and N. Tsourveloudis, "A UAV vision system for airborne surveillance," *IEEE International Conference on Robotics and Automation (ICRA)*, Vol. 1, 77–83, 2004.
14. Bhaskaranand, M. and J. D. Gibson, "Low-complexity video encoding for UAV reconnaissance and surveillance," *IEEE Military Communications Conference (MILCOM)*, 1633–1638, 2011.
15. Pinkney, M. F. J., D. Hampel, and S. DiPierro, "Unmanned

aerial vehicle (UAV) communications relay," *IEEE Military Communications Conference (MILCOM)*, Vol. 1, 47–51, 1996.

16. Zhan, P., K. Yu, and A. L. Swindlehurst, "Wireless relay communications with unmanned aerial vehicles: Performance and optimization," *IEEE Transactions on Aerospace and Electronic Systems*, Vol. 47, No. 3, 2068–2085, Jul. 2011.
17. Firouzeh, Z. H., M. Moradian, A. Safari-Hajat-Aghaei, and H. Mir-Mohammad-Sadeghi, "Design and implementation of ground station antennas for UAV data radio link in UHF band," *Information and Communication Technologies (ICTTA)*, Vol. 2, 2195–2200, 2006.
18. Gautier, W., A. Stehle, B. Schoenlinner, V. Ziegler, U. Prechtel, and W. Menzel, "RF-MEMS tunable filters on low-loss LTCC substrate for UAV data-link," *European Microwave Conference (EuMC)*, 1700–1703, 2009.
19. Sun, W. and Y. Hu, "Design and realization of direct PLL FM transmitter for UAV data link," *International Conference on Information Engineering (ICIE)*, Vol. 1, 522–525, 2009.
20. Moorehouse, D. M. and A. Humen, *Improved UAV Datalink Performance Using Embedded Antennas,* Nurad Technologies, Web, Maryland, 2012.
21. Chen, J., Q. Fei, and Q. Geng, "The design of data link for multi-UAVs," *4th International Conference on Intelligent Human-Machine Systems and Cybernetics (IHMSC)*, Vol. 1, 106–109, 2012.
22. "Mini telemaster kit V2 from hobby lobby," Online Available: http://www.hobby-lobby.com/telemaster_mini_v2_1037035_prd1.htm, Accessed: Oct. 09, 2012.
23. Sharawi, M. S., O. A. Rawashdeh, and D. N. Aloi, "Performance of an embedded monopole antenna array in a UAV wing structure," *15th IEEE Mediterranean Electrotechnical Conference (MELECON)*, 835–838, 2010.
24. Sharawi, M. S., D. N. Aloi, and O. A. Rawashdeh, "Design and implementation of embedded printed antenna arrays in small UAV wing structures," *IEEE Transactions on Antennas and Propagation*, Vol. 58, No. 8, 2531–2538, Aug. 2010.
25. Quan, X. L., R.-L. Li, J. Y. Wang, and Y. H. Cui, "Development of a broadband horizontally polarized omnidirectional planar antenna and its array for base stations," *Progress In Electromagnetics Research*, Vol. 128, 441–456, 2012.
26. Wang, W.-B., Q. Feng, and D. Liu, "Synthesis of thinned linear

and planar antenna arrays using binary PSO algorithm," *Progress In Electromagnetics Research*, Vol. 127, 371–387, 2012.

27. Lee, W.-S., K.-S. Oh, and J.-W. Yu, "A wideband planar monopole antenna array with circular polarized and band-notched characteristics," *Progress In Electromagnetics Research*, Vol. 128, 381–398, 2012.
28. Ibrahim, M., S. Deif, and M. S. Sharawi, "A 14-element printed planar antenna array embedded within a UAV structure," *Antennas and Propagation Conference (LAPC)*, 1–4, Loughborough, 2012.
29. Tsuji, H., D. Gray, M. Suzuki, and R. Miura, "Radio location estimation experiment using array antennas for high altitude platforms," *IEEE 18th International Symposium on Personal, Indoor and Mobile Radio Communications (PIMRC)*, 1–5, 2007.
30. Chamberlain, N., M. Zawadzki, G. Sadowy, E. Oakes, K. Brown, and R. Hodges, "The UAVSAR phased array aperture," *IEEE Aerospace Conference,* 13, 2006.
31. Park, P.-J., S.-M. Choi, D.-H. Lee, and B.-S. Lee, "Performance of UAV (unmanned aerial vehicle) communication system adapting WiBro with array antenna," *11th International Conference on Advanced Communication Technology (ICACT)*, Vol. 02, 1233–1237, 2007.
32. Pettersson, L., R. Gunnarsson, O. Lunden, S. Leijon, and A. Gustafsson, "Experimental investigation of a smoothly curved antenna array on a UAV-nose mock-up," *Proceedings of the Fourth European Conference on Antennas and Propagation (EuCAP)*, 1–5, 2010.
33. "SCN-3-28+," Online Available: http://www.minicircuits.com/MCLStore/ModelInfoDisplay?13581288891780.9941441877971389, Accessed: Jan. 14, 2013.
34. "BP4U1+," Online Available: http://www.minicircuits.com/MCLStore/ModelInfoDisplay?13581289653080.23021050564588463, Accessed: Jan. 14, 2013.
35. "ANSYS HFSS," Online Available: http://www.ansys.com/Products/Simulation+Technology/Electromagnetics/High-Performance+Electronic+Design/ANSYS+HFSS, Accessed: Jan. 26, 2013.
36. "MATLAB — The language of technical computing," Online Available: http://www.mathworks.com/products/matlab/, Accessed: Nov. 26, 2012.